Rotation, Electric-Field Responses, and Absolute Enantioselection in Chiral Crystals

Rikuto Oiwa and Hiroaki Kusunose
Department of Physics, Meiji University, Kawasaki 214-8571, Japan

(Received 14 March 2022; accepted 3 August 2022; published 8 September 2022)

The microscopic origin of chirality, possible electric-field induced static rotational lattice deformation, and rotation-field induced electric polarization are investigated. By building up a realistic tight-binding model for the elemental Te crystal in terms of a symmetry-adapted basis, we identify the microscopic origin of the chirality and essential couplings among polar and axial vectors with the same time-reversal properties. Based on this microscopic model, we elucidate quantitatively that an interband process, driven by nearest-neighbor spin-dependent imaginary hopping, is the key factor in the electric-field induced rotation and its inverse response. From the symmetry point of view, these couplings and responses are characteristic and common to any chiral material, leading to a possible experimental approach to achieve absolute enantioselection by simultaneously applied electric and rotation fields, or a magnetic field and electric current, and so on, as a conjugate field of the chirality.

DOI: 10.1103/PhysRevLett.129.116401

Introduction.—Chirality is three-dimensional geometric property exhibiting ubiquitously in nature. Handedness or enantiomer in chiral materials is characterized by a quantity having a time-reversal $\mathcal{T}$-even pseudoscalar (spatial-inversion $\mathcal{P}$ odd) property [1,2], whose sign corresponds to left or right handedness. This significant quantity in chiral materials, however, has not fully been understood at the microscopic level. Thus, clarifying the microscopic origin of a $\mathcal{T}$-even pseudoscalar inherent in chiral materials is essential to unveiling the heart of chirality and to achieving absolute enantioselection in chiral materials.

In this Letter, we begin with an introductory discussion of the features of $\mathcal{T}$-even pseudoscalar and important coupling to it based on the symmetry argument. Then, to confirm the existence of the coupling, we quantitatively investigate the expected responses by using the specific microscopic model of the elemental Te crystal. Lastly, we propose a possible experimental approach to realize absolute enantioselection in chiral materials, by the external fields that are accessible to the $\mathcal{T}$-even pseudoscalar via the elucidated coupling.

Chirality and related quantities.—The $\mathcal{T}$-even pseudoscalar has the same symmetry properties of the inner product of polar and axial vectors with the same $\mathcal{T}$ property. This is clearly discussed by the concept of electronic multipole basis [3–6]. Namely, a $\mathcal{T}$-even pseudoscalar corresponds to an electric toroidal (ET) monopole G_0 with $(\mathcal{P},\mathcal{T})=(-,+)$, which is an "order parameter" of the chirality since it becomes the totally symmetric irreducible representation (IR) when a system belongs to a crystallographic point group with proper rotations only (see Table XVI in Ref. [4]). Since an inner product of a magnetic (M) dipole $\boldsymbol{M}$, $(\mathcal{P},\mathcal{T})=(+,-)$, and magnetic toroidal (MT) dipole $\boldsymbol{T}$, $(\mathcal{P},\mathcal{T})=(-,-)$ belongs to the same IR of G_0, there can exist an invariant coupling,

$$gG_0(\boldsymbol{T}\cdot\boldsymbol{M}), \tag{1}$$

in the sense of Landau free energy, where g is a coupling constant. As an electric current $\boldsymbol{J}$ induces its conjugate quantity $\boldsymbol{T}$, it also induces $\boldsymbol{M}$ through Eq. (1) in a chiral system with active G_0. Indeed, the current-induced optical activity [7] and the kinetic magnetoelectric (Edelstein) effect [8,9] were proposed and observed in the elemental Te crystal [10–12]. Similarly, the $\boldsymbol{k}$-space representation of G_0 [4], i.e., $\boldsymbol{k}\cdot\boldsymbol{\sigma}$, brings about the hedgehog spin texture observed around the H point of the Brillouin zone in Te [13,14].

An ET monopole G_0 can couple with in another way:

$$g'G_0(\boldsymbol{Q}\cdot\boldsymbol{G}), \tag{2}$$

where $\boldsymbol{Q}$ is an electric (E) dipole, $(\mathcal{P},\mathcal{T})=(-,+)$, such as a position vector $\boldsymbol{R}$, while $\boldsymbol{G}$ represents an ET dipole with $(\mathcal{P},\mathcal{T})=(+,+)$ [4]. Equation (2) implies that a $\boldsymbol{G}$-flux structure exists in chiral crystals as shown in Fig. 1(a), and the direction of the fluxes characterizes the handedness. Note that the $\boldsymbol{G}$ vector solely acts as the order parameter of the recently discovered ferro-axial (rotational) order in $\mathrm{RbFe(MoO_4)_2}$ [15] and $\mathrm{BaTiO_3}$ [16], and the antiferroaxial ordering in $\mathrm{Ba(TiO)Cu_4(PO_4)_4}$ [17]. The rotational-ordered systems are closely related to chiral systems through Eq. (2).

Since a classical representation of $\boldsymbol{G}$ is given by a vortexlike alignment of E dipoles $\boldsymbol{Q}$ as shown in Fig. 1(b), its conjugate field is a rotation of the electric field, $\boldsymbol{\omega}_{\mathrm{E}}=\boldsymbol{\nabla}\times\boldsymbol{E}$, which is equivalent to the time-dependent

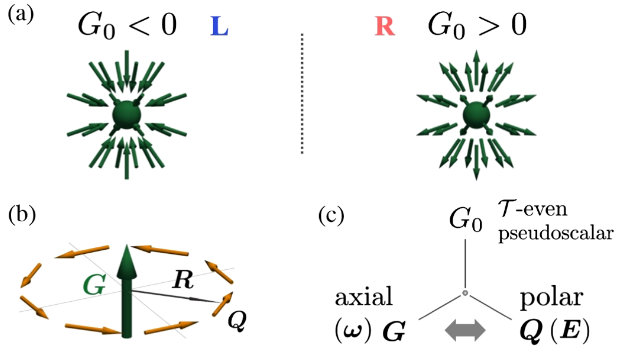

FIG. 1. (a) ET monopole G_0 in terms of the flux structure of the ET dipoles $\boldsymbol{G}$, whose direction determines the handedness of the chirality. (b) Classical view of the ET dipole, which is a vortexlike alignment of the E dipoles $\boldsymbol{Q}$. (c) The essential coupling existing in chiral crystals. The conjugate fields of $\boldsymbol{G}$ and $\boldsymbol{Q}$ are given in the parentheses.

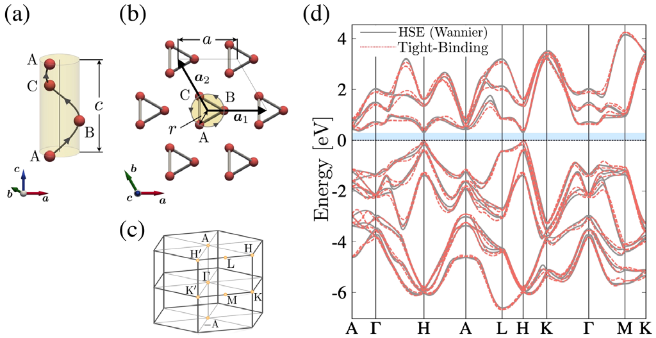

FIG. 2. (a) Crystal structure of the right-handed Te. (b) A unit cell contains A, B, and C sublattices along a helical chain. (c) First Brillouin zone of Te. (d) The comparison of the band dispersion between our TB model and DF calculation. The Fermi energy is taken as the origin, and the blue shaded area represents the insulating gap.

magnetic field through Maxwell's equation. Moreover, from the symmetry property of $\boldsymbol{G}$, a static rotational lattice deformation $\boldsymbol{\omega} = \boldsymbol{\nabla} \times \boldsymbol{u}$ ($\boldsymbol{u}$ is a displacement vector of atoms) could be an alternative conjugate field to $\boldsymbol{G}$, provided a proper electron-lattice coupling. From this relation, $\boldsymbol{G}$ is also significant in the transverse rotational phonon modes in both achiral [18–20] and chiral crystals [21–23].

As discussed above, there exists a third-order coupling in the free energy as shown in Fig. 1(c):

$$F^{(3)} = g_{\perp} G_0^{(1)} (G_x Q_x + G_y Q_y) + g_z G_0^{(2)} G_z Q_z, \quad (3)$$

where the coupling constants satisfy $g_z = g_{\perp}$ in cubic crystals; otherwise $g_z \neq g_{\perp}$ (z is along the screw axis). Here, $G_0^{(1)}$ and $G_0^{(2)}$ can be independent ET monopoles in general, and a coupling only with the vector product of electric degrees of freedom as Eq. (2) is written for simplicity. This coupling gives rise to a conversion from a polar field such as the electric field or temperature gradient into an axial response such as a static rotational lattice deformation, and vice versa. In other words, an electric-field induced rotation (EIR) and its inverse response, i.e., a rotation-field induced electric polarization (RIP), could appear in chiral crystals. Note that one can apply a rotational lattice deformation by using a transverse ultrasonic wave as it generates both the strain and rotation fields. The RIP (called rotoelectricity there) was already predicted by Gopalan and Litvin based on the symmetry argument [24]; however, its origin and the connection to the chirality remain unclear at the microscopic level. It should also be emphasized that the present EIR (static rotational deformation) is qualitatively different from a heat-current or electric-field induced phonon angular momentum, i.e., *dynamical* (time-reversal broken) lattice rotation, predicted by Hamada *et al.* [25,26].

In what follows, we elucidate the microscopic origin of G_0 and related responses, EIR and RIP, by taking Te as a specific example. First, we construct the realistic tight-binding (TB) model of Te by using the results of the density-functional (DF) calculation. Since the obtained TB model is expressed in terms of the symmetry-adapted electronic multipole basis, we can easily identify the microscopic origin of G_0 and evaluate the relevant couplings to it quantitatively. We then propose a possible experimental approach to achieve absolute enantioselection, keeping the coupling, Eq. (3), in mind.

Tight-binding model for Te.—Let us first consider the specific TB model for Te. As shown in Fig. 2(a), the bulk Te crystal consists of the threefold-symmetric helical chains, which contain A, B, and C sublattices in a unit cell as shown in Fig. 2(b). The space group of the right- and left-handed Te are P$3_1$21 (#152, D_3^4) and P$3_2$21 (#154, D_3^6), respectively. Hereafter, we focus on the right-handed Te. The lattice constants are $a = 4.458$ Å and $c = 5.925$ Å, and the relaxed value is $u = r/a = 0.274$ for the dimensionless helix parameter [27], where r denotes the radius of the helix.

Since the electronic states near the band edges (Fermi level) in Te mainly consist of three p orbitals, p_x, p_y, and p_z [28], we consider the spinful TB Hamiltonian in an 18×18 matrix. The TB Hamiltonian is constructed by using the symmetry-adapted multipole basis Z_α [4–6] as $\mathcal{H} = \sum_\alpha z_\alpha Z_\alpha$, where Z_α are the independent multipole basis satisfying the orthonormalization, $\mathrm{Tr}(Z_\alpha Z_\beta) = \delta_{\alpha\beta}$. Note that each Z_α belongs to the totally symmetric IR of D_3^4, i.e., A_1, and it is expressed by the direct product of the cluster or bond basis [29,30] and atomic basis as shown later [31,32]. They are generated automatically by the symbolic computation with symmetry operations [33]. Then, the coefficients z_α ($\Delta_i^Q, \lambda_i^Q, t_i^Q, \alpha_i^Q, \ldots$) are determined so as to reproduce the band dispersions obtained by the DF calculation with the help of the machine-learning technique [33–37]. In this model construction, terms containing G_0 are particularly important.

The constructed TB Hamiltonian is expressed as $\mathcal{H}_0 = \mathcal{H}_{\rm CEF} + \mathcal{H}_{\rm SOC} + \sum_{i=1}^{8} \mathcal{H}_t^{(i)}$, where $\mathcal{H}_{\rm CEF}$ and $\mathcal{H}_{\rm SOC}$ are the crystalline electric field (CEF) and spin-orbit coupling (SOC) within the unit cell, and $\mathcal{H}_t^{(i)}$ is the ith neighbor hopping term. By taking up to the 8th neighbors, we achieved an accuracy less than 10^{-4} of the mean squared error between the normalized energy eigenvalues of our TB model and the DF result [33]. The comparison of the energy dispersions is shown in Fig. 2(d). We have also confirmed that the orbital and spin characters of the obtained electronic states roughly reproduce those obtained by DF calculation. Eventually, there are 255 independent parameters z_α in total, and 30 parameters are within the nearest-neighbor (NN) hopping: 4 CEF parameters, 5 SOC parameters, and 21 NN intrachain hopping parameters [33].

Among these multipole bases, the most dominant contributions containing the ET monopole are $G_{0\perp}^{(\rm ca)}$ in $\mathcal{H}_{\rm SOC}$ and $G_{0z}^{(\rm ba)}$, $G_{0\perp}^{(\rm ba)}$ in $\mathcal{H}_t^{(1)}$, which are given by (see the Supplemental Material for details [33])

$$G_{0\perp}^{(\rm ca)} = \frac{1}{\sqrt{2}} (Q_x^{(\rm c)} \otimes G_x^{(\rm a)} + Q_y^{(\rm c)} \otimes G_y^{(\rm a)}), \tag{4}$$

$$G_{0z}^{(\rm ba)} = T_z^{(\rm b)} \otimes \sigma_z^{(\rm a)}, \tag{5}$$

$$G_{0\perp}^{(\rm ba)} = \frac{1}{\sqrt{2}} (T_x^{(\rm b)} \otimes \sigma_x^{(\rm a)} + T_y^{(\rm b)} \otimes \sigma_y^{(\rm a)}), \tag{6}$$

where the superscripts (c, b, and a) represent cluster, bond, and atomic basis, respectively. The weight of $G_{0\perp}^{(\rm ca)}$ is $\lambda_1^G = 1.718$ eV which is the most dominant contribution among $\mathcal{H}_{\rm CEF} + \mathcal{H}_{\rm SOC}$, and that of $G_{0z}^{(\rm ba)}$ is $\alpha_2^G = 1.749$ eV which is the most dominant contribution among the ET monopoles in $\mathcal{H}_t^{(t)}$, while that of $G_{0\perp}^{(\rm ba)}$ is $\alpha_3^G = 0.5854$ eV. Note that $G_{0z}^{(\rm ca)}$ does not appear because the z component of the E dipole $Q_z^{(\rm c)}$ identically vanishes in the present Hilbert space [33]. We have confirmed that the magnitude of the parameters decreases for further neighbor hoppings [33]. Here, $\boldsymbol{G}^{(\rm a)} = \boldsymbol{l} \times \boldsymbol{\sigma}$ is the atomic ET dipole ($\boldsymbol{l}$ and $\boldsymbol{\sigma}$ are the dimensionless orbital and half of spin angular momenta, respectively). $Q_\mu^{(\rm c)}$ ($\mu = x, y$) and $T_\mu^{(\rm b)}$ ($\mu = x, y, z$) are the μ components of the cluster E dipole and bond MT dipole, which are defined in the ABC sublattice space as

$$Q_x^{(\rm c)} = \frac{1}{\sqrt{6}} \begin{pmatrix} -1 & 0 & 0 \\ 0 & 2 & 0 \\ 0 & 0 & -1 \end{pmatrix}, \quad Q_y^{(\rm c)} = \frac{1}{\sqrt{2}} \begin{pmatrix} -1 & 0 & 0 \\ 0 & 0 & 0 \\ 0 & 0 & 1 \end{pmatrix}, \tag{7}$$

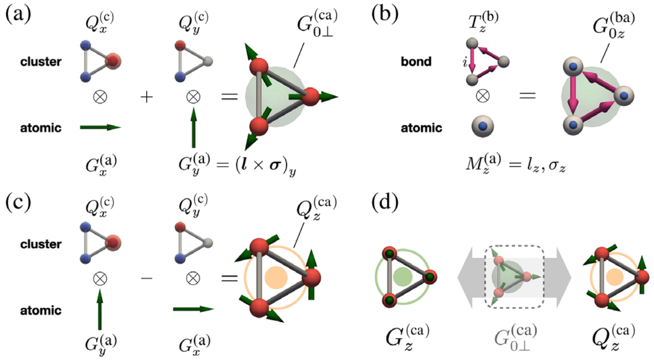

FIG. 3. Schematic picture of multipole basis for Te. (a) Local ET monopole, $G_{0\perp}^{(\rm ca)}$, (b) itinerant ET monopole, $G_{0z}^{(\rm ba)}$, and (c) local E dipole, $Q_z^{(\rm ca)}$. (d) The interparity coupling between the ET dipole $G_z^{(\rm ca)}$ and E dipole $Q_z^{(\rm ca)}$ via $G_{0\perp}^{(\rm ca)}$.

$$Q_0^{(\rm c)} = \frac{1}{\sqrt{3}} \begin{pmatrix} 1 & 0 & 0 \\ 0 & 1 & 0 \\ 0 & 0 & 1 \end{pmatrix}, \quad T_z^{(\rm b)} = \frac{1}{\sqrt{6}} \begin{pmatrix} 0 & -i & i \\ i & 0 & -i \\ -i & i & 0 \end{pmatrix}, \tag{8}$$

$$T_x^{(\rm b)} = \frac{1}{2} \begin{pmatrix} 0 & -i & 0 \\ i & 0 & i \\ 0 & -i & 0 \end{pmatrix}, \quad T_y^{(\rm b)} = \frac{1}{2\sqrt{3}} \begin{pmatrix} 0 & -i & -2i \\ i & 0 & -i \\ 2i & i & 0 \end{pmatrix}. \tag{9}$$

$Q_\mu^{(\rm c)}$ with diagonal elements correspond to the on site potentials, while $T_\mu^{(\rm b)}$ with off-diagonal elements represent an imaginary hopping among A, B, and C sublattices [33]. Although there are also the spinless version of $G_{0z}^{(\rm ba)}$ and $G_{0\perp}^{(\rm ba)}$ which are given by replacing $\boldsymbol{\sigma}$ with $\boldsymbol{l}$ in Eqs. (5) and (6), the weight of these multipole bases is much smaller than that for the spinful ones. As shown in Fig. 3(a) and Eq. (2), $G_{0\perp}^{(\rm ca)}$ is the local ET monopole having the $\boldsymbol{G}^{(\rm a)}$-flux structure in the unit cell. On the other hand, $G_{0z}^{(\rm ba)}$ in Fig. 3(b) is the itinerant ET monopole which is a kind of SOC with the spin-dependent imaginary hopping. From Figs. 3(a) and 3(b), the relation between the sign of G_0 and the handedness is apparent. For example, in Fig. 3(b), $T_z^{(\rm b)}$ corresponds to the imaginary hopping directed to the $+z$ direction for the right-handed system. If we consider the left-handed system, $T_z^{(\rm b)}$ directs to the $-z$ direction, and the sign of G_0 is inverted.

These ET monopoles, $G_{0z}^{(\rm ba)}$ and $G_{0\perp}^{(\rm ca)}$, play the roles of $G_0^{(1)}$ and $G_0^{(2)}$ in Eq. (3), respectively. As discussed below, both of them give dominant contributions to the EIR and RIP. In addition, the itinerant ET monopole $G_{0z}^{(\rm ba)}$ is also the main origin of the Edelstein effect observed in Te [11,12]. Moreover, the Fourier transform of $G_{0z}^{(\rm ba)}$ together with

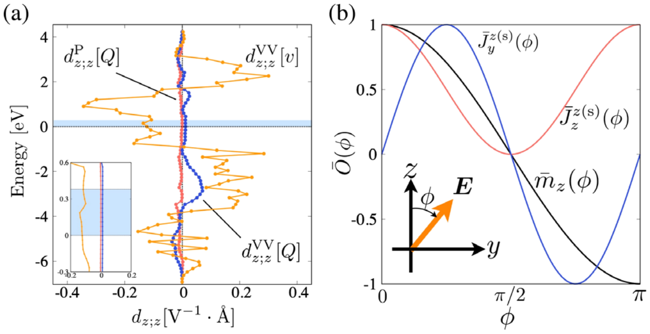

FIG. 4. (a) Chemical potential μ dependence of $d^{\mathrm{P}}_{z;z}$ and $d^{\mathrm{VV}}_{z;z}$ with Eqs. (11), (12), and (13) at $T = 0.01$ eV, and $N = 64^3$. The inset shows the enlarged plot near the Fermi level. (b) The electric-field angle dependence of the spin current in the yz plane $\bar{J}^{z(\mathrm{s})}_{z}(\phi) \propto \cos^2(\phi)$ and $\bar{J}^{z(\mathrm{s})}_{y}(\phi) \propto \sin(2\phi)$, and the magnetization due to the Edelstein effect, $\bar{m}_z(\phi) \propto \cos(\phi)$. $\bar{O}(\phi)$ denotes the normalized value of $O(\phi)$ by its absolute maximum value.

$G^{(\mathrm{ba})}_{0\perp}$ gives rise to the hedgehog spin texture around the H point in momentum space [13,14,33].

Electric-field induced rotation.—As already discussed phenomenologically, a conversion between polar and axial degrees of freedom is expected to occur in chiral materials via Eq. (3). To demonstrate it microscopically, we investigate the electric-field induced ET dipole response based on the present TB model. Before showing the results, we define explicitly the local E- and ET-dipole operators that describe the input and output of the response. The E dipole $Q^{(\mathrm{ca})}_{z}$ is given by the similar expression of Eq. (4) with a minus sign for the second term, which is schematically shown in Fig. 3(c), i.e., the vortexlike alignment of $G^{(\mathrm{a})}_{x}$ and $G^{(\mathrm{a})}_{y}$ [cf. the roles of $\boldsymbol{G}$ and $\boldsymbol{Q}$ are exchanged in Fig. 1(b)]. The static rotational response is also described by $G^{(\mathrm{ca})}_{z} = Q^{(\mathrm{c})}_{0} \otimes G^{(\mathrm{a})}_{z}$.

Using the Kubo formula, the response function in $G^{(\mathrm{ca})}_{z} = d_{z;z}E_z$ is expressed as (c is the lattice constant) [33]

$$d_{z;z} = d^{\mathrm{P}}_{z;z}[Q] + d^{\mathrm{VV}}_{z;z}[Q] + d^{\mathrm{VV}}_{z;z}[v], \tag{10}$$

$$d^{\mathrm{P}}_{z;z}[Q] = \frac{ec}{N}\sum_{\boldsymbol{k}nm}^{\epsilon_{n\boldsymbol{k}}=\epsilon_{m\boldsymbol{k}}} \frac{\partial f_{n\boldsymbol{k}}}{\partial \epsilon_{n\boldsymbol{k}}} G^{nm}_{z\boldsymbol{k}} Q^{mn}_{z\boldsymbol{k}}, \tag{11}$$

$$d^{\mathrm{VV}}_{z;z}[Q] = \frac{ec}{N}\sum_{\boldsymbol{k}nm}^{\epsilon_{n\boldsymbol{k}}\neq\epsilon_{m\boldsymbol{k}}} \frac{f_{n\boldsymbol{k}} - f_{m\boldsymbol{k}}}{\epsilon_{n\boldsymbol{k}} - \epsilon_{m\boldsymbol{k}}} G^{nm}_{z\boldsymbol{k}} Q^{mn}_{z\boldsymbol{k}}, \tag{12}$$

$$d^{\mathrm{VV}}_{z;z}[v] = -\frac{e\hbar}{iN}\sum_{\boldsymbol{k}nm}^{\epsilon_{n\boldsymbol{k}}\neq\epsilon_{m\boldsymbol{k}}} \frac{f_{n\boldsymbol{k}} - f_{m\boldsymbol{k}}}{(\epsilon_{n\boldsymbol{k}} - \epsilon_{m\boldsymbol{k}})^2} G^{nm}_{z\boldsymbol{k}} v^{mn}_{z\boldsymbol{k}}. \tag{13}$$

Here, the matrix element of an operator is $O^{nm}_{i\boldsymbol{k}} = \langle\psi_{n\boldsymbol{k}}|\hat{O}_i|\psi_{m\boldsymbol{k}}\rangle$, $f_{n\boldsymbol{k}} = f(\epsilon_{n\boldsymbol{k}})$ is the Fermi distribution function, e (> 0) is the elementary charge, and N is the number of lattice sites. The responses $d^{\mathrm{P}}_{z;z}$ and $d^{\mathrm{VV}}_{z;z}$ represent the intraband Pauli contribution proportional to the density of states (DOS), and interband van Vleck contributions, respectively. $[Q]$ and $[v]$ indicate the contributions arising from the local E dipole and itinerant hopping process via the velocity operator $\boldsymbol{v}_{\boldsymbol{k}} = \partial\mathcal{H}_0/\partial\hbar\boldsymbol{k}$, respectively. Note that $d^{\mathrm{P}}_{z;z}[v]$ vanishes identically due to the time-reversal symmetry. We have used $N = 64^3$ and the temperature $T = 0.01$ eV in the following results.

Figure 4(a) shows the chemical potential μ dependence of the responses. The interband contribution from the itinerant hopping process $d^{\mathrm{VV}}_{z;z}[v]$ is always dominant irrespective of μ, and the EIR occurs even in the insulator. Note that the EIR and RIP could occur in any chiral insulators, which are qualitatively different from the kinetic magnetoelectric (Edelstein) effect expected only in metals due to its intraband origin. Analyzing the essential parameters to exhibit the finite response $d_{z;z}$ [32], it turns out that the lowest order of the response is proportional to the highest-weight term $G^{(\mathrm{ba})}_{0z}$ of $\mathcal{H}_0$ with the coefficient α^G_2 [33]. This is consistent with the fact that $d^{\mathrm{VV}}_{z;z}[v]$ is dominant in the numerical result. Thus, the itinerant ET monopole $G^{(\mathrm{ba})}_{0z}$ is the key component of the EIR response in Te. Note that the inverse RIP process is also expected to occur in both metals and insulators, as their response functions are common with Eqs. (11) and (12).

Although we have concentrated on the electronic responses above, the actual rotational lattice deformation should occur via the electron-lattice coupling. When we restrict our discussion to a rotational lattice deformation with the angle ω_z with respect to the z screw axis, the electron-lattice coupling can be evaluated by rotating inversely the electronic system by the angle $-\omega_z$ [38–40]. Namely, $\mathcal{H}^{(z)}_{\text{el-rot}} = e^{-ij^{(\mathrm{ca})}_{z}\omega_z}\mathcal{H}_0 e^{ij^{(\mathrm{ca})}_{z}\omega_z} - \mathcal{H}_0 = i[\mathcal{H}_0, j^{(\mathrm{ca})}_{z}]\omega_z + \cdots$, where $j^{(\mathrm{ca})}_{z} = Q^{(\mathrm{c})}_{0} \otimes (l_z + \sigma_z/2)$ is the total angular momentum. We find the most important contribution from the $\lambda^G_1 G^{(\mathrm{ca})}_{0\perp}$ term in $\mathcal{H}_0$ as

$$\mathcal{H}^{(z)}_{\text{el-rot}} \sim \lambda^G_1 Q^{(\mathrm{ca})}_{z}\omega_z, \tag{14}$$

with $\lambda^G_1 = 1.718$ eV. Similarly, the perpendicular components are obtained, and they are a factor $1/\sqrt{2}$ smaller than $\mathcal{H}^{(z)}_{\text{el-rot}}$. This term directly causes the electric polarization by applying a lattice rotation field with the use of transverse ultrasound wave for instance.

The induced electronic ET dipole can also be observed by the spin-current measurement. When the induced ET dipole by the electric field E_z is present, two types of nonlinear spin currents are expected: $J^{z(\mathrm{s})}_{z} = \sigma^{z(\mathrm{s})}_{z;zz}E_z^2$ and $J^{z(\mathrm{s})}_{y} = \sigma^{z(\mathrm{s})}_{y;yz}E_yE_z$, where $J^{\nu(\mathrm{s})}_{\mu} \equiv (J_\mu\sigma_\nu + \sigma_\nu J_\mu)/2$ is the spin current operator where J_μ is the electric current

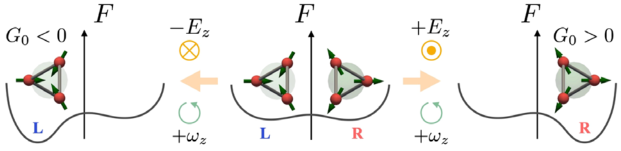

FIG. 5. Free-energy differences for absolute enantioselection under simultaneous application of rotation (ω_z) and electric (E_z) fields. The sign of $\omega_z E_z$ controls the preferred handedness during the crystallization process.

operator. As shown in Fig. 4(b), the electric-field angle ϕ dependences of $J_\mu^{\nu(\mathrm{s})}$ in the yz plane are given by $J_z^{z(\mathrm{s})}(\phi) \propto \cos^2(\phi)$ and $J_y^{z(\mathrm{s})}(\phi) \propto \sin(2\phi)$, respectively. Note that they are in marked contrast to that of the magnetization due to the Edelstein effect, $m_z(\phi) = \alpha_{z;z}^{(\mathrm{J})} E_z \propto \cos(\phi)$. Thus, the electric-field induced ET dipole is verifiable by examining the ϕ dependence of $J_z^{z(\mathrm{s})}(\phi)$ and $J_y^{z(\mathrm{s})}(\phi)$.

Absolute enantioselection by rotation and electric fields.—Finally, we propose a possible experimental approach to achieve absolute enantioselection in chiral materials, without the use of seed crystals [41]. As was shown phenomenologically and microscopically, there is a proper coupling among G_0, $\boldsymbol{G}$, and $\boldsymbol{Q}$ in chiral materials. The conjugate field of $\boldsymbol{Q}$ is an electric field $\boldsymbol{E}$ and that of $\boldsymbol{G}$ is a rotation field $\boldsymbol{\omega}$ such as a rotation of electric field or equivalently time-dependent magnetic field. Thus, the conjugate field of chirality, that is G_0, is a product of polar and axial vector fields, E_μ and ω_μ. In the electromagnetism, it is known as a quantity called zilch, which describes optical chirality [42]. Therefore, as shown in Fig. 5 in the case of $\mu = z$, absolute enantioselection can be achieved by simultaneous application of electric (E_μ) and rotation (ω_μ) fields for instance. The sign of $\omega_\mu E_\mu$ controls the preferred handedness during the crystallization process, as shown in the left-most and right-most panels in Fig. 5. It should be emphasized that a time-dependent magnetic field is favorable with the constant time derivative or net accumulation with a definite sign. In addition to this, both electric and magnetic fields must be parallel with each other. Moreover, as was discussed in Eq. (1), G_0 could also couple with $M_\mu T_\mu$. Thus, the combined static magnetic field and time-dependent electric field (i.e., $\boldsymbol{\nabla} \times \boldsymbol{B}$, which is a conjugate field of T_μ), or the combined static magnetic field and electric current can be used to achieve absolute enantioselection as well. This generic approach is applicable to any chiral material.

Summary.—We have unveiled the microscopic origin of chirality and possible electric-field induced static rotational lattice deformation and its inverse response, rotation-field induced electric polarization. First, based on the symmetry, we have argued that the chirality corresponds to the electric toroidal monopole, which couples with the G_0-type quantities as in Eqs. (1)–(3). Note that their conjugate fields are the electric and magnetic parts of the optical zilch [42] for instance. Thus, the essential couplings as in Eqs. (1)–(3), which arise from the higher-order coupling of our TB Hamiltonian, are the key elements for both the electric-field induced rotation and its inverse response. Using the realistic tight-binding model for the elemental Te crystal, we have elucidated that an interband process, driven by the itinerant electric toroidal monopole shown in Fig. 3(b), is the crucial factor in these response functions. These responses occur even in the insulators, which is in marked contrast to the kinetic magnetoelectric (Edelstein) effect observed in Te. Lastly, we have proposed a generic experimental approach to realize the absolute enantioselection in chiral materials by the conjugate field of the chirality, such as simultaneously applied electric and rotation fields, or the magnetic field and electric current, and so on. Since the larger magnitude of a coupling between G_0 and its conjugate field is favorable for efficient achievement of an absolute enantioselection, the quantitative experimental observation of the responses related to the coupling is crucially important in future development.

The authors would like to thank Yuki Yanagi for providing us the data of the DF calculation. We also thank Michito Suzuki, Hiroaki Ikeda, Yoshihiko Togawa, Junichiro Kishine, Koichi Izawa, Hiroshi Amitsuka, Tatsuya Yanagisawa, Hiroyuki Hidaka, and Satoru Hayami for fruitful discussions. This work was supported by JSPS KAKENHI Grants No. JP19K03752, No. JP20J21838, and No. JP21H01031. Some of the numerical and symbolic calculations were performed in the supercomputing systems in the MAterial science Supercomputing system for Advanced MUlti-scale simulations towards NExt-generation-Institute for Materials Research (MASAMUNE-IMR) of the Center for Computational Materials Science, Institute for Materials Research, Tohoku University.

[1] L. D. Barron, *Molecular Light Scattering and Optical Activity*, 2nd ed. (Cambridge University Press, Cambridge, England, 2004).
[2] L. D. Barron, Rend. Fis. Acc. Lincei **24**, 179 (2013).
[3] S. Hayami and H. Kusunose, J. Phys. Soc. Jpn. **87**, 033709 (2018).
[4] S. Hayami, M. Yatsushiro, Y. Yanagi, and H. Kusunose, Phys. Rev. B **98**, 165110 (2018).
[5] H. Watanabe and Y. Yanase, Phys. Rev. B **98**, 245129 (2018).
[6] H. Kusunose, R. Oiwa, and S. Hayami, J. Phys. Soc. Jpn. **89**, 104704 (2020).
[7] L. E. Vorob'ev, E. L. Ivchenko, G. E. Pikus, I. I. Farbshteĭn, V. A. Shalygin, and A. V. Shturbin, JETP Lett. **29**, 441 (1979), https://ui.adsabs.harvard.edu/abs/1979JETPL..29..441V.
[8] T. Yoda, T. Yokoyama, and S. Murakami, Sci. Rep. **5**, 12024 (2015).

[9] T. Yoda, T. Yokoyama, and S. Murakami, Nano Lett. **18**, 916 (2018).

[10] V. A. Shalygin, A. N. Sofronov, L. E. Vorob'ev, and I. I. Farbshtein, Phys. Solid State **54**, 2362 (2012).

[11] T. Furukawa, Y. Shimokawa, K. Kobayashi, and T. Itou, Nat. Commun. **8**, 954 (2017).

[12] T. Furukawa, Y. Watanabe, N. Ogasawara, K. Kobayashi, and T. Itou, Phys. Rev. Research **3**, 023111 (2021).

[13] M. Hirayama, R. Okugawa, S. Ishibashi, S. Murakami, and T. Miyake, Phys. Rev. Lett. **114**, 206401 (2015).

[14] M. Sakano *et al.*, Phys. Rev. Lett. **124**, 136404 (2020).

[15] W. Jin, E. Drueke, S. Li, A. Admasu, R. Owen, M. Day, K. Sun, S.-W. Cheong, and L. Zhao, Nat. Phys. **16**, 42 (2020).

[16] T. Hayashida, Y. Uemura, K. Kimura, S. Matsuoka, D. Morikawa, S. Hirose, K. Tsuda, T. Hasegawa, and T. Kimura, Nat. Commun. **11**, 4582 (2020).

[17] T. Hayashida, K. Kimura, D. Urushihara, T. Asaka, and T. Kimura, J. Am. Chem. Soc. **143**, 3638 (2021).

[18] L. Zhang and Q. Niu, Phys. Rev. Lett. **115**, 115502 (2015).

[19] H. Chen, W. Zhang, Q. Niu, and L. Zhang, 2D Mater. **6**, 012002 (2018).

[20] H. Zhu, J. Yi, M.-Y. Li, J. Xiao, L. Zhang, C.-W. Yang, R. A. Kaindl, L.-J. Li, Y. Wang, and X. Zhang, Science **359**, 579 (2018).

[21] J. Kishine, A. S. Ovchinnikov, and A. A. Tereshchenko, Phys. Rev. Lett. **125**, 245302 (2020).

[22] Y. Chen, M. Kadic, and M. Wegener, Nat. Commun. **12**, 3278 (2021).

[23] K. Ishito, H. Mao, Y. Kousaka, Y. Togawa, S. Iwasaki, T. Zhang, S. Murakami, J. ichiro Kishine, and T. Satoh, arXiv:2110.11604.

[24] V. Gopalan and D. B. Litvin, Nat. Mater. **10**, 376 (2011).

[25] M. Hamada, E. Minamitani, M. Hirayama, and S. Murakami, Phys. Rev. Lett. **121**, 175301 (2018).

[26] M. Hamada and S. Murakami, Phys. Rev. B **101**, 144306 (2020).

[27] N. Bouad, L. Chapon, R.-M. Marin-Ayral, F. Bouree-Vigneron, and J.-C. Tedenac, J. Solid State Chem. **173**, 189 (2003).

[28] M. Cheng, S. Wu, Z.-Z. Zhu, and G.-Y. Guo, Phys. Rev. B **100**, 035202 (2019).

[29] M.-T. Suzuki, T. Koretsune, M. Ochi, and R. Arita, Phys. Rev. B **95**, 094406 (2017).

[30] M.-T. Suzuki, H. Ikeda, and P. M. Oppeneer, J. Phys. Soc. Jpn. **87**, 041008 (2018).

[31] S. Hayami, Y. Yanagi, and H. Kusunose, Phys. Rev. B **102**, 144441 (2020).

[32] R. Oiwa and H. Kusunose, J. Phys. Soc. Jpn. **91**, 014701 (2022).

[33] See Supplemental Materials at http://link.aps.org/supplemental/10.1103/PhysRevLett.129.116401, The definition of the symmetry-adapted multipole basis and their construction procedure are given in Sec. I; A brief description of the parameter fitting, and the obtained values of the 30 parameters within the nearest-neighbor hopping are also given in Sec. II, which includes Refs. [36–38]; The number of independent parameters is determined by the total number of the independent base Z_α belonging to A_1 irreducible representation. It depends on not only the size of the Hamiltonian matrix, but also the number of neighboring sites. Within the nearest-neighbor hopping, there are 30 parameters; The essential multipole basis that give rise to the hedgehog spin texture around the H point of the Brillouin zone in Te is shown in Sec. III; The crystallographic symmetry constraints on the response function of the electric-field induced electric toroidal dipole is shown in Sec. IV; The dominant contribution to the electric-field induced electric toroidal dipole ($\boldsymbol{G}$) is shown in Sec. V.

[34] J. Paier, M. Marsman, K. Hummer, G. Kresse, I. C. Gerber, and J. G. Ángyán, J. Chem. Phys. **124**, 154709 (2006).

[35] V. B. Anzin, M. I. Eremets, Y. V. Kosichkin, A. I. Nadezhdinskii, and A. M. Shirokov, Phys. Status Solidi A **42**, 385 (1977).

[36] S. S. Tsirkin, P. A. Puente, and I. Souza, Phys. Rev. B **97**, 035158 (2018).

[37] Z. Wang, S. Ye, H. Wang, J. He, Q. Huang, and S. Chang, npj Comput. Mater. **7**, 11 (2021).

[38] T. Goto, A. Tamaki, T. Fujimura, and H. Unoki, J. Phys. Soc. Jpn. **55**, 1613 (1986).

[39] T. Kuromaru, H. Kusunose, and Y. Kuramoto, J. Phys. Soc. Jpn. **70**, 521 (2001).

[40] R. Kurihara, K. Mitsumoto, M. Akatsu, Y. Nemoto, T. Goto, Y. Kobayashi, and M. Sato, J. Phys. Soc. Jpn. **86**, 064706 (2017).

[41] Y. Kousaka, T. Koyama, K. Ohishi, K. Kakurai, V. Hutanu, H. Ohsumi, T. Arima, A. Tokuda, M. Suzuki, N. Kawamura, A. Nakao, T. Hanashima, J. Suzuki, J. Campo, Y. Miyamoto, A. Sera, K. Inoue, and J. Akimitsu, Phys. Rev. Mater. **1**, 071402(R) (2017).

[42] I. Proskurin, A. S. Ovchinnikov, P. Nosov, and J. Kishine, New J. Phys. **19**, 063021 (2017).